JACS
JOURNAL OF THE AMERICAN CHEMICAL SOCIETY
Article
pubs.acs.org/JACS

A (3 + 3)-Dimensional "Hypercubic" Oxide-Ionic Conductor: Type II Bi_2O_3–Nb_2O_5

Chris D. Ling,*[,†] Siegbert Schmid,[†] Peter E. R. Blanchard,[†] Vaclav Petříček,[§] Garry J. McIntyre,[‡,△] Neeraj Sharma,[†,^] Andrey Maljuk,[¶] Aleksey A. Yaremchenko,[#] Vladislav V. Kharton,[#] Matthias Gutmann,[⊥] and Ray L. Withers[∞]

[†]School of Chemistry, The University of Sydney, Sydney NSW 2006, Australia
[§]Institute of Physics, ASCR, v.v.i., The Academy of Sciences of the Czech Republic, 182 21 Prague 8, Czech Republic
[‡]Institut Laue-Langevin, BP 156, 38042 Grenoble Cedex 9, France
[¶]Leibniz Institute for Solid State and Materials Research Dresden, Helmholtzstrasse 20, D-01069 Dresden, Germany
[#]Department of Materials and Ceramic Engineering, CICECO, University of Aveiro, 3810-193 Aveiro, Portugal
[⊥]ISIS, Science and Technology Facilities Council, Rutherford Appleton Laboratory, Didcot, OX11 0QX, United Kingdom
[∞]Research School of Chemistry, Australian National University, Canberra ACT 0200, Australia

Supporting Information

ABSTRACT: The high-temperature cubic form of bismuth oxide, δ-Bi_2O_3, is the best intermediate-temperature oxide-ionic conductor known. The most elegant way of stabilizing δ-Bi_2O_3 to room temperature, while preserving a large part of its conductivity, is by doping with higher valent transition metals to create wide solid-solutions fields with exceedingly rare and complex (3 + 3)-dimensional incommensurately modulated "hypercubic" structures. These materials remain poorly understood because no such structure has ever been quantitatively solved and refined, due to both the complexity of the problem and a lack of adequate experimental data. We have addressed this by growing a large (centimeter scale) crystal using a novel refluxing floating-zone method, collecting high-quality single-crystal neutron diffraction data, and treating its structure together with X-ray diffraction data within the superspace symmetry formalism. The structure can be understood as an "inflated" pyrochlore, in which corner-connected NbO_6 octahedral chains move smoothly apart to accommodate the solid solution. While some oxide vacancies are ordered into these chains, the rest are distributed throughout a continuous three-dimensional network of wide δ-Bi_2O_3-like channels, explaining the high oxide-ionic conductivity compared to commensurately modulated phases in the same pseudobinary system.

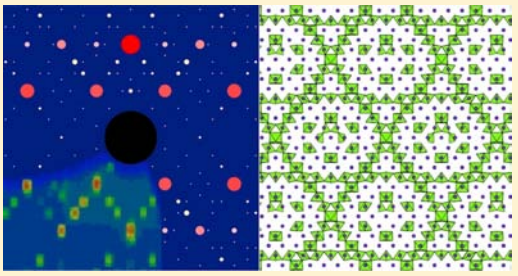

INTRODUCTION

The search for new and improved solid-state oxide-ionic conductors, principally for use as fuel-cell and oxygen-separation membranes, is one of the biggest motivators of research in materials chemistry.[1−3] The best-performing material at high temperatures is cubic δ-Bi_2O_3, with oxide-ionic conductivity of 1−1.5 S cm^{-1} at 730−830 °C,[4,5] compared to ∼0.01 S cm^{-1} for optimally doped yttria-stabilized zirconia ($Zr_{1-x}Y_xO_{2-x/2}$, x = 0.16) at 730 °C.[6] Unfortunately, however, on cooling to the intermediate-temperature regime desired for most electrochemical applications (400−650 °C), δ-Bi_2O_3 transforms to the structurally distinct α phase via intermediate β or γ phases, dramatically reducing the conductivity and creating strain that would fatally compromise the structural integrity of films or ceramics used in any working devices. Consequently, other high-performing cubic systems, notably those based on CeO_2,[7] currently receive more attention at the boundary of pure and applied research.

The exceptionally high oxide-ionic conductivity of δ-Bi_2O_3 is due to the 25% oxygen vacancies evenly distributed throughout its disordered fluorite-type structure.[5] Lower-temperature polymorphs eliminate these vacancies. Nevertheless, the fluorite-type average structure of δ-Bi_2O_3 (along with a significant fraction of its conductivity) can be preserved to room temperature by doping with smaller rare earth or higher-valent transition-metal cations [for reviews see e.g. refs 4 and 8−11]. The best results have been achieved by combinations of the two, notably $Bi_{12.5}La_{1.5}ReO_{24.5}$.[12]

The purely transition metal-doped δ-Bi_2O_3 phases show lower electrochemical performance than the rare earth-doped phases because the former tend to form ordered superstructures (although ionic conductivities of greater than 0.1 S cm^{-1} at 700 °C have been reported[11,13,14]). However, they are the most fascinating from a crystal-chemical point of view. Most

Received: November 11, 2012
Published: April 9, 2013

   dx.doi.org/10.1021/ja3109328 | J. Am. Chem. Soc. 2013, 135, 6477−6484

significantly, the Bi_2O_3–Nb_2O_5,[10,15−17] Bi_2O_3–Ta_2O_5,[10,18] Bi_2O_3–CrO_3,[19] and Bi_2O_3–MoO_3[20] pseudobinary systems all contain (3 + 3)-dimensional incommensurately modulated solid-solution phases, which are extremely rare—in fact, these doped bismuth oxides represent the majority of known cases to date. They were all identified as such by using electron diffraction, and while schematic models for their structures have been proposed based on supersymmetry constraints and local crystal-chemistry,[16,19,20] it has been impossible to refine any of those models due to a lack of quantitative experimental data. Crystallographically, they must be described in six dimensions by using the superspace-symmetry formalism. The only freely refined (3 + 3)-D structures have been those of wüstite ($Fe_{1-x}O$)[21] and the mineral lazurite (ideally $Na_6Ca_2[Al_6Si_6O_{24}][SO_4,S]_2$),[22] both against single-crystal X-ray diffraction data. An overview of incommensurate compounds with (3 + 3)-dimensional modulations was very recently presented by van Smaalen et al.[23]

Solving and refining these structures is not a purely academic exercise. Because they are cubic, they are good models for pure δ-Bi_2O_3, which can only be approached by using disordered crystallographic[24] or total scattering[25,26] methods to find the long-range average structure, or in combination with computer simulations.[27,28] The details of the (3 + 3)-D ordered phases should shed light on the true local structure of δ-Bi_2O_3. They may also help understand and mitigate against process by which the disordered rare earth-doped phases evolve over the course of repeated cycling into ordered phases with much lower conductivity.

The most heavily studied of the (3 + 3)-D phases is Type II Bi_2O_3–Nb_2O_5, first recognized by Miida and Tanaka,[29] which has the widest solid-solution range (~10–25% mole Nb_2O_5) and the highest ionic conductivity[14,30−32] as well as attractive dielectric[33] and photocatalytic[34,35] properties. At the Nb-rich end of this solid solution, Type II is only thermodynamically stable at high temperatures (above ~930 °C for 25% mole Nb_2O_5),[36,37] although for less than ~20% mole Nb_2O_5 it appears to be stable to room temperature. Below this phase boundary, the commensurately modulated Type III phase is thermodynamically preferred, with an ordered tetragonal 3 × 3 × 7 superstructure of δ-Bi_2O_3.[38] However, even at Nb-rich compositions, Type II is easily quenched to room temperature due to the very slow kinetics of the reconstructive phase transition, requiring a lengthy induction time in the order of 10 h, even at 800 °C.[36] Most importantly, at these compositions the incommensurate Type II exhibits higher oxide ionic conductivity at all temperatures than the commensurate Type III phase;[37] i.e., (3 + 3)-D incommensurability appears to enhance the desired physical properties of this system. All of this underlies the need to quantitatively solve—and understand—the details of what is arguably the most complex type of ordered structure possible.

EXPERIMENTAL SECTION

Single-phase polycrystalline samples of Type II and III Bi_2O_3–Nb_2O_5, both of nominal composition $(Bi_2O_3)_{0.76}(Nb_2O_5)_{0.24}$, were prepared by solid-state synthesis in air from Bi_2O_3 and Nb_2O_5 (>99.99% purity). The stoichiometric mixture was ground in an agate mortar and pestle and calcined at 1373 K for 100 h with several regrindings to yield a pure sample of cubic Type II according to X-ray powder diffraction (XRD) data. Part of this sample was then annealed at 1173 K for a further 100 h to yield a pure sample (also confirmed by XRD) of the Type III phase.

The volatility of Bi_2O_3 at high temperatures, the wide solid-solution range, the fact that the material melts incongruently according to Roth and Waring,[39] and the need to quench through the transition to Type III all conspire against the growth of single crystals of Type II Bi_2O_3–Nb_2O_5 with use of conventional slow-cooling or flux-growth methods. We overcame those obstacles through the use of the crucible-free floating-zone technique in a unique "refluxing" mode. In preparation for floating-zone growth, a polycrystalline feed rod of the Type II phase 6 mm in diameter was pressed at 60 MPa in a hydrostatic press and then sintered at 1373 K for 1 h in a vertical tube furnace. The crystal was grown in air, using an NEC double-mirror type image furnace equipped with 500 W halogen lamps. A rapid growth rate of 10 mm h^{-1} was used in an attempt to minimize the loss of Bi_2O_3 through volatilization. Indeed, following initial melting of the seed and feed rods and the establishment of a moderately stable molten zone, it immediately became clear that Bi_2O_3 was evaporating and that the molten zone was becoming unstable. However, after approximately 15 min, it was observed that crystalline Bi_2O_3 needles were recondensing on the upper part of the feed rod, approximately 10 mm above the molten zone. As the growth proceeded and the feed rod moved downward, these needles remelted and ran back into the molten zone. A Bi_2O_3 reflux state was thus established, which remained stable for 2 h (20 mm of growth) until the top of the feed rod was observed and the growth terminated. Such a high-temperature oxide reflux has, to the best of our knowledge, never been described before in the literature. The boule thus obtained was transparent yellow, 6 mm in diameter, and 20 mm long. On removal from the furnace it developed cracks and broke into pieces up to 4 mm in diameter.

Preliminary single-crystal neutron diffraction data were collected from pieces of the crystal boule on the time-of-flight instrument SXD at ISIS (Rutherford Appleton Laboratories, UK). Data were collected at room temperature at three different crystal orientations with exposure times ranging from 9 to 21 h. The wavelength-sorted white-beam time-of-flight technique combined with large area-detector coverage allows the recording of a large volume in reciprocal space. Although extensive overlap of satellite reflections precluded quantitative data integration, this experiment was successful in establishing that the boule consisted exclusively of the Type II phase, and in identifying a high-quality roughly spherical (~4 mm diameter) single crystal for further analysis.

Monochromatic (λ = 0.9461 Å) single-crystal neutron diffraction data were subsequently collected at room temperature from this crystal on the instrument D19 at the Institut Laue-Langevin (France). Slightly less than a full quadrant of reciprocal space out to 0.93 $Å^{-1}$ in sin θ/λ was scanned, equivalent to 16 asymmetric reciprocal volumes. Inspection of the data showed that satellite reflections were visible around all fundamental face-centered cubic reflections hkl, at positions $(h + m\varepsilon)\boldsymbol{a}^* + (k + n\varepsilon)\boldsymbol{b}^* + (l + p\varepsilon)\boldsymbol{c}^*$ where $\boldsymbol{a}^*$, $\boldsymbol{b}^*$, and $\boldsymbol{c}^*$ are the reciprocal unit-cell axes of the cubic average structure, the magnitude of the primary wave-vectors $\varepsilon \approx 0.38$, and m, n, and p are all even or all odd irrespective of the (common) parity of h, k, and l as required by the $P{:}Fm\ \bar{3}m{:}Fd\bar{3}m$ superspace group symmetry.[15] No satellite reflections of significant intensity were observed for $m^2 + n^2 + p^2 > 8$, which still resulted in 26 satellite reflections around each fundamental reflection. Reconstructed and schematic experimental precession images are shown in Figure 1. Details of the data reduction process, in which 11816 reflections reduced to 725 unique reflections (a redundancy of 16.298) with an internal agreement of R_{int} = 2.11% [1.47% for the 4524 reflections with $I > 3\sigma(I)$], are presented in the Supporting Information.

Following the collection of neutron diffraction data, the crystal was broken and a small piece (approximately 0.001 mm^3) used to collect X-ray diffraction data on a Bruker–Nonius APEX-II X-ray diffractometer with Mo Kα radiation (λ = 0.71073 Å). Due to the extremely high X-ray absorption of bismuth, these data were of significantly lower quality than the neutron data, as judged by the internal agreement factor on merging equivalent reflections. Unsurprisingly, given the very different relative scattering powers of the constituent elements, the hierarchy of satellite intensities was found to be different compared to the neutron data set. In particular, it

dx.doi.org/10.1021/ja3109328 | J. Am. Chem. Soc. 2013, 135, 6477−6484

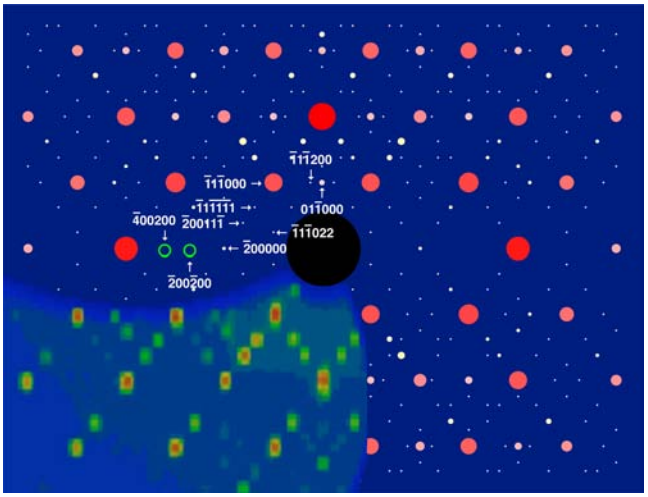

Figure 1. ⟨110000⟩* precession image (bottom left quadrant) reconstructed (at reduced resolution) from single crystal neutron diffraction data (D19@ILL), overlaid on a schematic representation of the observed ($I > 3\sigma I$) Bragg peaks where intensities are proportional to the size and color (red > yellow > white) of the spots. Selected peaks including ⟨*hkl*002⟩*, ⟨*hkl*022⟩*, and ⟨*hkl*111⟩* type satellites are indexed. Green circles highlight satellites that are absent due to the *d*-hyperglide extinction condition $F\langle hk0mn0\rangle^* = 0$ unless $m + n = 4J$, where J is an integer.

was possible to integrate ⟨*hkl*222⟩* type satellites with $I > 3\sigma(I)$, none of which reached this criterion for observation using neutrons. Details of the data reduction process, in which 13945 reflections reduced to 624 unique reflections (a redundancy of 22.348) with an internal agreement of R_{int} = 9.45% [8.91% for the 2555 reflections with $I > 3\sigma(I)$], are presented in the Supporting Information.

Dense ceramics of Type II and III samples were prepared for ionic-conductivity measurements by pressing disk- and bar-shaped samples uniaxially at 250 MPa and sintering at 1373 K for 10 h in air, followed by polishing and deposition of porous Pt electrodes. Then the samples were annealed at 1133−1173 and 1213−1233 K in air for Type III and II, respectively; the presence of single phases was validated by XRD in each case. The pellets were found to be >90% of theoretical density for both compounds.

Total (ionic + electronic) conductivity, σ, was determined by AC impedance spectroscopy (HP4284A precision LCR meter, 20 Hz−1 MHz) and a four-probe DC technique in air. Oxide-ion-transference numbers (t_O) shown in Figure 2a were determined by the modified electromotive force (EMF) method,[40] taking electrode polarization into account. Determination of the average ion-transference numbers was performed at 1093−1253 K under O_2/air gradient. Prior to electrical measurements, the dense ceramic samples were additionally annealed at temperatures ensuring the formation of single Type II and III phases over 25−50 h; the measurements in relevant temperature ranges were performed in both heating and cooling regimes in order to check reproducibility and to validate an absence of hysteresis phenomena. Within the specific temperature ranges where Type II and Type III phases exist, the regimes included 30−45 min dwells for equilibration at each temperature; the steps and heating/cooling rate were 20 and 3 K min^{-1}, respectively. The partial oxide-ionic (σ_O) and electronic (σ_e) conductivities shown in Figure 2b were calculated from the data on total conductivity and ion-transference numbers.

Niobium K-edge X-ray absorption near-edge spectra (XANES) shown in Figure 3 for Type II and Type III Bi_2O_3−Nb_2O_5 were collected on Beamline 20B at the Photon Factory, Japan. Powder samples were sandwiched between Kapton tape and positioned in front of the X-ray beam. A silicon (311) crystal monochromator provided a monochromatic flux of ∼6 × 10^{-11} photons/s, with a resolution of ±1 eV at 1 KeV and a beam size of 200 × 8000 μm. Transmission spectra were measured in a Kr-filled ionization chamber

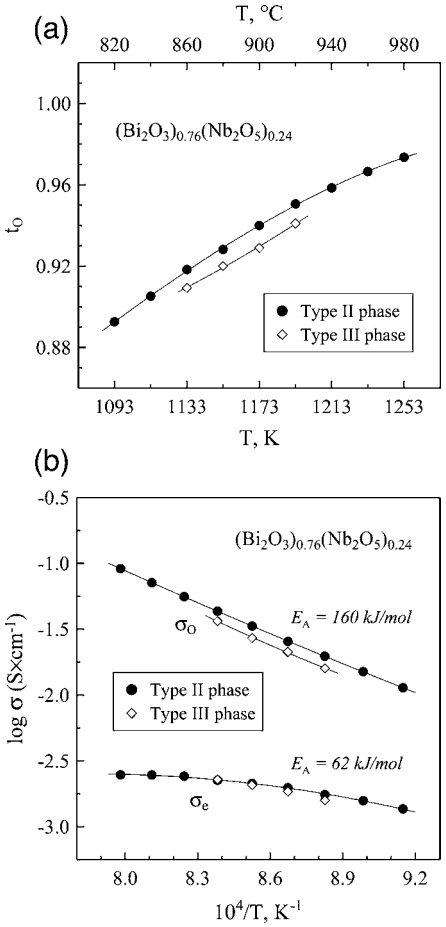

Figure 2. (a) Oxide ion-transference numbers for the ceramic sample of Type II and Type III $(Bi_2O_3)_{0.76}(Nb_2O_5)_{0.24}$, determined by the modified EMF technique under O_2/air gradient. (b) Partial oxide-ionic (σ_O) and electronic (σ_e) conductivities for the ceramic samples of Type II and Type III $(Bi_2O_3)_{0.76}(Nb_2O_5)_{0.24}$, calculated from the data on total conductivity and ion-transference numbers.

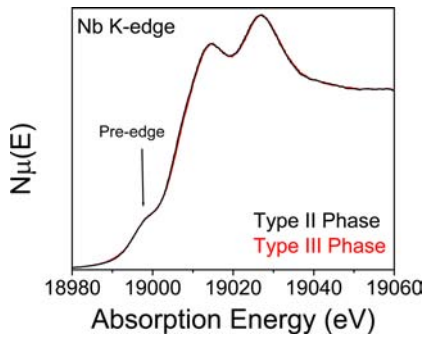

Figure 3. Nb K-edge spectra for the Type II (black) and Type III (red) phases. All spectra were collected in transmission mode. Note that the lines are almost perfectly overlapped.

while the fluorescence spectra were measured with a 36-element fluorescence detector. Through the absorption edge, spectra were collected at 0.25 eV per step. The energy scale was calibrated by using the K-edge of a pure Nb foil at 18 986 eV. All XANES spectra were analyzed with the Athena software program.[41]

RESULTS

Structure refinements used the program Jana2006.[42] The starting model consisted of only the two independent atoms

dx.doi.org/10.1021/ja3109328 | J. Am. Chem. Soc. 2013, 135, 6477−6484

of the fluorite-type average structure: a mixed-metal (Bi/Nb) site and a partially occupied oxygen site, both of which were modeled with anisotropic atomic displacement parameters (ADPs). The (3 + 3)-D superspace symmetry and resulting constraints on the atomic modulation functions (AMFs) to be determined have been described in detail previously.[16] The superspace group symmetry used can be written as $Fm\bar{3}m(\alpha,\alpha,\alpha)q00(\alpha,-\alpha,-\alpha)q00(-\alpha,\alpha,-\alpha)000$ (number 225.3.215.8), using the notation recently introduced by Stokes, Campbell, and van Smaalen.[43] A full list of equivalent positions, symmetry operators, and extinction conditions for this superspace group is presented in Table S1 of the Supporting Information. This corresponds in the supercentering description to a nonstandard centering with 12 centering vectors, describing *F*-centering among the main reflections, satellite reflections, and combinations thereof. Alternatively, in the relatively intuitive notation of Yamamoto, the superspace group symmetry can be described as $P{:}Fm\bar{3}m{:}Fd\bar{3}m$.[21] The superspace group was confirmed in the neutron and X-ray data-reduction steps, where no reflections with $I > 3\sigma I$ were observed to break the corresponding extinction condition $F\langle hk0mn0\rangle^* = 0$ unless $m + n = 4J$, where J is an integer.

Given the circumstances of the growth, the final composition of the grown boule obviously cannot be assumed to be the same as that of the feed rod. Indeed, using Vegard's law in conjunction with our original study of the Type II solid solution,[10] the refined lattice parameters $a = 5.4790(1)$ Å and $\varepsilon = 0.377(1)$ indicate a slightly more bismuth-rich composition $(Bi_2O_3)_{0.795}(Nb_2O_5)_{0.205}$ (or $Bi_{3.18}Nb_{0.82}O_{6.82}$, $Z = 4$, with respect to the nominal composition of the feed material Bi_3NbO_7). The overall composition was fixed at this value.

Due to the relative insensitivity of neutron diffraction data to the difference between Bi and Nb (neutron scattering lengths of 8.532 and 7.054 fm, respectively), a preliminary refinement of the metal atom array was first carried out against the X-ray data set. In addition to a scale factor and Type-II extinction parameter, 20 occupational, 20 positional, and 20 ADP modulation waves were refined for the mixed-metal site. The X-ray data being relatively insensitive to modulations of the much lighter oxygen atoms, these were left on their average fluorite-type positions. For the metal atoms, the occupational modulation waves were found to be far stronger than the positional or ADP waves. Figure 4 shows part of the refined distribution of metal sites that are more than 50% occupied by Nb within the fluorite-type array. When lines are drawn between nearest-neighbor Nb atoms, a strong structural motif emerges of continuous chains of Nb sites along ⟨110000⟩ directions, intersecting to form an open framework, with a relatively small number of additional Nb sites in between.

The significant difference in the quality of the X-ray and neutron data sets, combined with the very different way in which X-rays (scattered by electron density) and neutrons (scattered by nuclear density) respond to thermal and static disorder of a crystal lattice—Debye–Waller factors—unfortunately destabilized all attempts at a combined "X+N" refinement. Therefore, the metal atom array refined against X-ray data was used as a starting point for the final refinement of the structure against neutron diffraction data. The most important part of this array, the occupational modulation (described by three independent parameters), was fixed at the X-ray refined result, while the positional and ADP parts were allowed to refine. Due to the lack of any observed $\langle hkl222\rangle^*$-type reflections in the neutron data set, the number of modulation waves on these refined parts was reduced from 20 to 16. Sixteen occupational, 16 positional, and 16 ADP modulation waves were also refined for the oxygen site, in addition to a scale factor and Type-I extinction parameter.

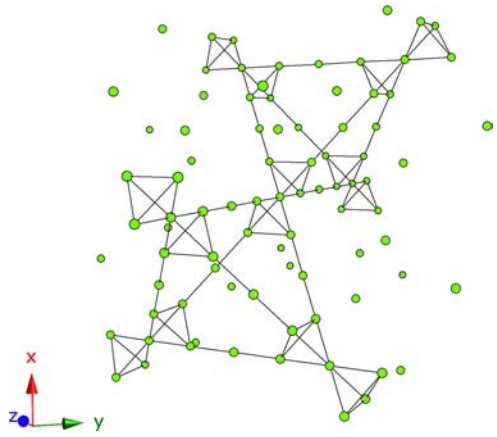

Figure 4. Perspective view of the network of metal atom sites more than 50% occupied by Nb in 3 × 3 × 3 fluorite-type subcells of Type II $(Bi_2O_3)_{0.795}(Nb_2O_5)_{0.205}$, obtained by refinement against single-crystal X-ray diffraction data. Lines are drawn between nearest neighbor Nb sites (along ⟨110000⟩ directions).

Careful analysis of Fourier maps revealed significant nuclear density around the oxygen site, which was not accounted for in the model. This density appeared to be due to static disorder rather than displacive modulations. In the final stage of refinement, therefore, fourth-order anharmonic ADPs were introduced on the oxygen site, along with 16 modulation waves for each of the two additional parameters required to describe those ADPs.

Details of the data collection (Table S2), refinement statistics (Table S3), symmetry constraints and refinement results (Tables S4 and S5), and a list of observed and calculated intensities used in the refinement (Table S6) have been deposited as Supporting Information.

The total and partial (oxide-ionic and electronic) conductivities shown in Figure 2 confirm that the conductivity is predominantly oxide ionic. A minor electronic contribution decreases with increasing temperature. The Type III phase exhibits a lower ionic contribution to the total conductivity than the Type II phase. Within experimental error, the partial electronic conductivities of the Type II and III phases are almost equal. The activation energy (E_A) values for partial oxide-ionic conduction are also similar for both phases, 160 ± 3 kJ mol^{-1}. E_A for electronic transport was substantially lower, 62 kJ mol^{-1} at 1093–1213 K. The latter value is in excellent agreement with literature data on similar compounds studied in the low-temperature range,[44] i.e., 60 kJ mol^{-1}.

The XANES spectra for the Type II and III phases were essentially identical (Figure 3). Given that the pre-edge feature in particular, corresponding to a dipole-forbidden 1*s*-to-4*d* transition,[45] is incredibly sensitive to local distortions and coordination number,[46] this indicates that Nb atoms occupy similar local coordination environments (predominantly octahedral) in both phases.

DISCUSSION

The crystal chemistry of stabilized δ-Bi_2O_3-related phases in the Bi_2O_3–Nb_2O_5 system was first described by Zhou et al., on the basis of high-resolution transmission electron microscopy

dx.doi.org/10.1021/ja3109328 | J. Am. Chem. Soc. 2013, 135, 6477–6484

(HRTEM), as being driven by the formation of tetrahedral clusters of corner-sharing NbO_6 octahedra.[15,17] We later proposed[47] that it is instead driven by the formation of corner-sharing NbO_6 octahedral chains running along $\langle 110\rangle_f$ directions of the fluorite-type subcell, a model which is also consistent with the $\langle 110\rangle_f$ projection HRTEM images presented by Zhou et al. and which has since been supported by vibrational spectroscopic data.[48] Both phenomenologies are based on the relationship between fluorite and pyrochlore types, and when taken to their logical conclusions at high Nb doping, both would result in a (hypothetical) pyrochlore $Bi_2Nb_2O_6$. The distortion of the fluorite-type lattice around a tetrahedral cluster of NbO_6 octahedra (which would also occur at the intersection of four $\langle 110\rangle_f$ chains), due to the strong preference of Nb^{5+} for 6-fold octahedral coordination over 8-fold cubic coordination, is shown schematically in Figure 5.

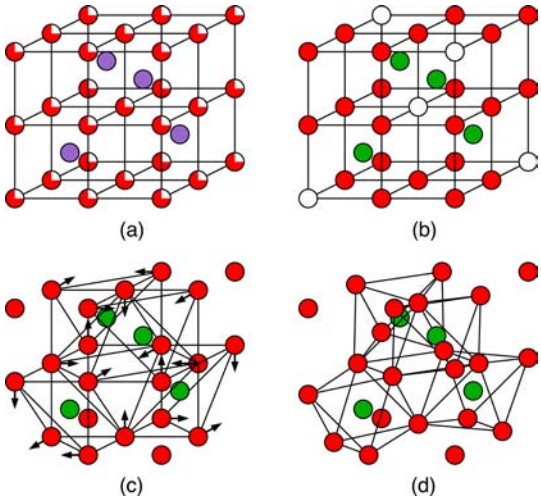

Figure 5. Scheme showing how tetrahedral clusters of NbO_6 octahedra can be incorporated into the fluorite-type average structure of niobium-doped δ-Bi_2O_3. The volumes shown are equivalent to one unit cell. (a) A unit cell of δ-Bi_2O_3 showing a statistical distribution of 25% vacancies (white) on the oxygen (red) atoms coordinating bismuth (purple) atoms. (b) The ordering of oxygen vacancies surrounding a tetrahedron of niobium atoms (green), reducing the cubic coordination to octahedral coordination. (c) Cooperative displacive relaxations of remaining oxygen atoms around niobium atoms. (d) The resulting tetrahedron of octahedra.

We demonstrated the validity and predictive power of this phenomenology by using it to construct a model for the commensurate ($3 \times 3 \times 7$) Type III superstructure,[38] which produced perfect fits to synchrotron X-ray and neutron powder diffraction data after minimal Rietveld refinement. Applying the same approach to Type II Bi_2O_3–Nb_2O_5 predicts a structure that can be thought of as a three-dimensionally expanded pyrochlore, where the $\langle 110\rangle_f$ chains of NbO_6 octahedra remain intact but are pulled apart from one another.[16] Tetrahedra (or triangles) of NbO_6 octahedra would still be found at the intersections of these chains as in Figure 5, but as the Nb content decreases from a hypothetical $Bi_2Nb_2O_6$ pyrochlore, these intersections become less common and isolated straight sections of chains start to predominate. These structural motifs can be clearly seen in the refined Nb atom array presented in Figure 4. Crystallographically, this is equivalent to placing NbO_6 octahedral chains within the volume defined by a so-called "D" periodic nodal surface (PNS),[49,50] mapped onto the three-dimensional space of the fluorite-type substructure.

Figure 6 shows representative *t*-plots[51] of the occupancy, bond lengths to coordinating oxygen atoms, and bond valence

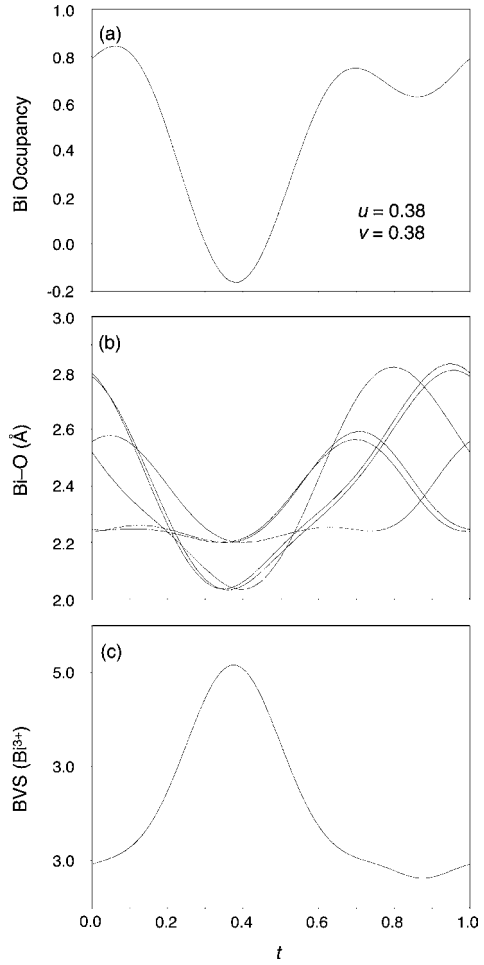

Figure 6. Variation in the fractional occupancy, bond lengths to oxygen atoms, and bond valence sum (BVS) for bismuth in Type II $(Bi_2O_3)_{0.795}(Nb_2O_5)_{0.205}$, as a function of the incommensurate parameter *t*,[51] when $u = v = 0.38$.

sum (BVS)[52] for Bi in the mixed-metal site in the final refined structure of $(Bi_2O_3)_{0.795}(Nb_2O_5)_{0.205}$. The minimum occupancy, minimum (and most regular) Bi–O distances, and maximum BVS all occur at $t = u = v = 0.38$, corresponding to the expected $\langle 110\rangle_f$ chains of NbO_6 octahedra in real space. The Bi occupancy necessarily passes slightly below 0 at the strongest point of its modulation, due to fact that only a finite number of modulation waves could be refined.

A representative part ($8 \times 8 \times 8$ fluorite-type subcells) of the final refined structure of $(Bi_2O_3)_{0.795}(Nb_2O_5)_{0.205}$ is shown in Figure 7a. The fractional occupancy cutoff for labeling a site as Nb vs Bi (or O vs a vacancy) was set to $^1/_2$. Nb–O bonds of less than 2.25 Å are drawn. It can clearly be seen that (a) O atoms in the vicinity of Nb atoms move away from their average fluorite-type positions and toward the Nb atoms and (b) O atom vacancies are concentrated around Nb sites, reducing their coordination numbers below 8. Both effects serve to create relatively ordered octahedral coordination environments around Nb, compared to the disordered cubic coordination environments in the average fluorite-type

dx.doi.org/10.1021/ja3109328 | J. Am. Chem. Soc. 2013, 135, 6477–6484

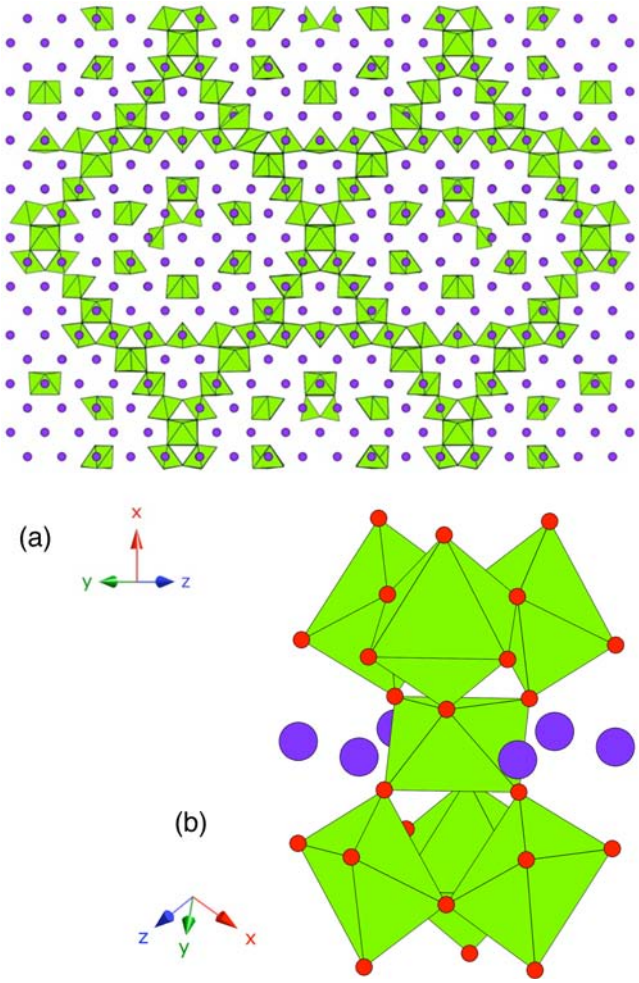

Figure 7. The final refined structure of Type II $(Bi_2O_3)_{0.795}(Nb_2O_5)_{0.205}$. (a) View along the ⟨110000⟩ direction, drawn over 8 × 8 × 8 fluorite-type subcells. The fractional occupancy cutoff for drawing atoms is $^1/_2$. Bi atoms are purple, and Nb atoms and polyhedra are green. (b) Close up of one of the pyrochlore-like clusters of NbO_6 octahedra found at the intersections of Nb ⟨110000⟩ chains, with O atoms in red (cf. Figure 1d).

structure; i.e., the occupational modulation waves on the metal atom site are in phase with the occupational and positional modulation waves on the oxygen site. The resulting chains of corner-connected NbO_x polyhedra along ⟨110000⟩ directions can clearly be seen, while the close-up in Figure 7b reveals pyrochlore-like clusters found at the intersections of those chains, as predicted by our model. Coordination environments around Bi are noticeably more irregular and asymmetric than around Nb, which may be accounted for to some extent by spatial localization of the stereochemically active $6s^2$ electron lone pair on Bi^{3+}.

Figure 8 shows a calculated Fourier map (which corresponds to nuclear density, having been obtained from the refinement against neutron diffraction data) for a single representative fluorite-type unit cell. The refined fourth-order anharmonic ADPs on the oxygen sites highlight the tendency of the oxygen atoms to move along ⟨110000⟩ directions, away from their average fluorite-type positions and toward pyrochlore-type positions.

The results of an unconstrained (3 + 3)-D refinement of the structure of Type II Bi_2O_3–Nb_2O_5 therefore bear out the

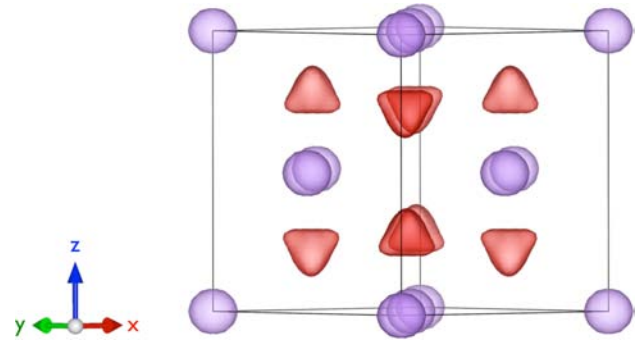

Figure 8. Calculated Fourier map for a single representative fluorite-type unit cell of Type II $(Bi_2O_3)_{0.795}(Nb_2O_5)_{0.205}$, from the final refinement against single-crystal neutron diffraction data (D19, ILL). Purple contours show the Bi/Nb nuclear density, and red contours show the O nuclear density. The results of refining fourth-order anharmonic ADPs on the O sites can be clearly seen, with nuclear density moving toward the faces of the Bi/Nb tetrahedron coordinating each O site.

phenomenological model in which it represents a smooth evolution from fluorite to pyrochlore. Figure 9 compares the

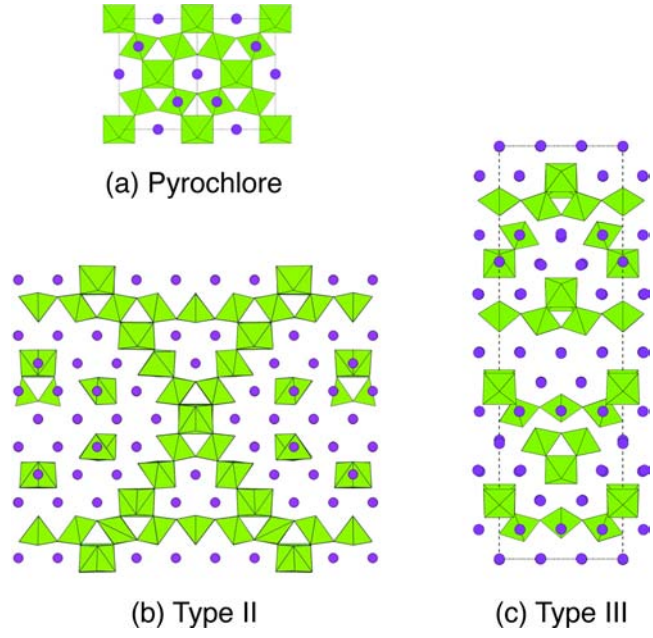

Figure 9. Views along equivalent $\langle 110 \rangle_f$ directions of (a) hypothetical pyrochlore-type $Bi_2Nb_2O_6$, (b) Type II $(Bi_2O_3)_{0.795}(Nb_2O_5)_{0.205}$, and (c) Type III $Bi_{94}Nb_{32}O_{221}$. Bismuth atoms are purple, and niobium atoms and polyhedra are green. Metal–oxygen bonds shorter than 2.25 Å are drawn.

structures of a hypothetical pyrochlore $Bi_2Nb_2O_6$ to the Type II "inflated" pyrochlore, in which Nb-rich chains with 6-fold antiprismatic coordination environments (approximating corner-connected octahedra, albeit highly distorted) move smoothly apart to accommodate the solid solution. Figure 9c shows that the commensurate low-temperature Type III structure also contains these chains, but they are only continuous along two of the four unique $\langle 110 \rangle_f$ directions, which lowers its symmetry from cubic to tetragonal. Note that our XANES experiment (Figure 3) confirmed that Nb atoms

dx.doi.org/10.1021/ja3109328 | J. Am. Chem. Soc. 2013, 135, 6477–6484

have identical (i.e., 6-fold) coordination environments in the Type II and Type III phases.

Figure 2 shows that the Type II phase exhibits a significantly higher oxide-ionic conductivity than the Type III phase. For comparison, the σ_O values at 1173 K are 0.033 and 0.027 S cm^{-1}, respectively. At the same time, the activation energies are almost equal, indicating that the ion-migration microscopic mechanisms and energetic barriers for anion jumps are very similar. This can be explained in terms of our refined structure, on the basis that conduction takes place primarily via bismuth-surrounded pathways in the partially disordered Birich channels along $\langle 110\rangle_f$ directions, in between the relatively well-ordered NbO_6 chains. Comparing the Type II and III structures (Figure 9), we note that Type II has much larger Birich channels, which are continuous along all four $\langle 110\rangle_f$ directions and thus form a large network of available pathways. The number of pathways surrounded by Bi^{3+} cations in the smaller, anisotropic channels of Type III is lower, leading to lower anion mobility with similar energetic barriers. Moreover, due to the relative proximity of these channels to NbO_6 octahedra, a larger fraction of anions in the Type III phase become immobile. It is relevant to note in this context that pure δ-Bi_2O_3, which could be thought of as having infinitely large and perfectly disordered Birich channels and thus continuous 3D network of the anion diffusion pathways, is a significantly better ionic conductor than both Types II and III.

The anharmonic ADPs shown in Figure 8, which could be refined due to the high quality of our single-crystal neutron diffraction data, provide further insight into this static disorder in the oxygen sublattice. They show oxygen atoms displacing from average fluorite-type positions toward pyrochlore-type positions, along $\langle 111\rangle_f$ directions. These anharmonic ADPs have essentially the same form as the oxygen nuclear-density maps obtained in recent studies of pure δ-Bi_2O_3 with use of reverse Monte Carlo[25] and maximum-entropy methods[26] to analyze total scattering in neutron powder diffraction data, as well as ab initio molecular dynamics.[27] Considering the topology of the structure and the breadth of the solid-solution range, it is clear that some static disorder of the cation sublattice must also necessarily be present; i.e., for incommensurate values of ε (which includes the entire experimentally observed composition range) there must always be some Bi atoms in the Nb chains, disrupting the local oxygen-ordering scheme and facilitating conduction. This type of disorder is not found in the less conductive Type III phase, where the chains are perfectly ordered (notwithstanding the small solid-solution range reported by Pirnat et al.[36]).

The presence of static disorder in the cation sublattice, and the possibility that samples synthesized in different ways (especially those quenched through the transition to Type III) could have different degrees of disorder, explains why the ionic conductivities reported here for $(Bi_2O_3)_{0.76}(Nb_2O_5)_{0.24}$ are significantly lower than some previous reports for Type II Bi_2O_3–Nb_2O_5, which includes values as high as 0.19 S cm^{-1} at 700 °C for $(Bi_2O_3)_{0.8}(Nb_2O_5)_{0.2}$ (Meng et al.[31]), 0.19 S cm^{-1} at 700 °C for $(Bi_2O_3)_{0.85}(Nb_2O_5)_{0.15}$ (Takahashi et al.[14]), 0.04 S cm^{-1} at 700 °C for $(Bi_2O_3)_{0.85}(Nb_2O_5)_{0.15}$ (Joshi et al.[30]), and even 0.64 S cm^{-1} at 730 °C for $(Bi_2O_3)_{0.85}(Nb_2O_5)_{0.15}$ (Yaremchenko et al.[32]). It should be noted that in the latter case, a fast degradation of the ionic conductivity with time was experimentally observed. The conductivity was found to decrease by a factor of 3–4 over 150–200 h, confirming the key role of the Types II ↔ III phase transformations in the intermediate-temperature range. Moreover, the initial conductivity values and degradation phenomena were reproducible after high-temperature treatments.

CONCLUSIONS

A remarkable feature of the (3 + 3)-D incommensurately modulated Type II Bi_2O_3–Nb_2O_5 phase is that it has the most complex type of ordered structure possible and yet, in terms of the number of free parameters not fixed by symmetry, it is also quite simple. For a description including fourth-order anharmonic ADPs, only 76 parameters needed to be refined (73 against neutron diffraction data, plus 3 describing the occupational modulation on the metal site that were fixed to the value refined against X-ray diffraction data). This can be compared to a nonmodulated refinement using the nearest commensurate approximate $\varepsilon = {}^3/_8$, giving an 8 × 8 × 8 supercell in $Fd\bar{3}m$, which would require 250 parameters using isotropic ADPs or 1361 using fourth-order anharmonic ADPs. The structure of Type II Bi_2O_3–Nb_2O_5 represents an elegant solution to the problem of accommodating dopants in a *long-range-ordered* manner without effectively lowering the symmetry from cubic. Most importantly, it preserves intact δ-Bi_2O_3-like regions in the form of wide and continuous channels, explaining the very high oxide-ionic conductivity. Given the apparent stability of the Type II phase, extending over a remarkably wide solid-solution range of 10–25% Nb doping, it is perhaps surprising that such infinitely adaptive, high-symmetry, modulated phases are not more common.

It is interesting that other (3 + 3)-D incommensurate phases in the transition metal-doped Bi_2O_3 systems [$Bi_{1-x}Ta_xO_{1.5+x}$ ($0.20 \le x \le 0.25$),[18] $Bi_{1-x}Mo_xO_{1.5+1.5x}$ ($x = 0.16$),[20] and $Bi_{1-x}Cr_xO_{1.5+1.5x}$ ($0.05 \le x \le 0.15$)[19]] have slightly different superspace group symmetries to the Nb-doped phase (the *d*-hyperglide being absent). Moreover, in the case of Cr-doping, there is clear spectroscopic evidence that Cr^{6+} ions have tetrahedral rather than octahedral coordination environments; and this is most likely also the case for Mo-doping, given that $Bi_{14}MoO_{24}$,[53,54] $Bi_{26}Mo_{10}O_{69}$,[55] and $Bi_{38}Mo_7O_{78}$[56] all have tetrahedrally coordinated Mo^{6+}. Thus, the crystal-chemical requirements of the dopant do not seem to be the most important factor in determining the superspace symmetry. An intriguing possibility that follows from this observation is that pure δ-Bi_2O_3 itself may dynamically accommodate oxide-ion vacancies in strings along $\langle 110\rangle_f$ directions as part of the conduction process, without giving rise to long-range-order and satellite reflections. Dopant cations (Nb, Ta, Mo, and Cr) may simply have the effect of pinning those vacancies and ordering them into octahedra or tetrahedra. Understanding the details of how dopant cations assert that order may therefore ultimately suggest rational routes to new and improved oxide-ionic conductors.

ASSOCIATED CONTENT

Supporting Information

Details of the single-crystal diffraction data reduction, superspace group symmetry (Table S1), collection (Table S2), statistics (Table S3), results (Tables S4 and S5), and a list of observed and calculated intensities (Table S6) for the final refinement against neutron diffraction data of the (3 + 3)-dimensional modulated structure of Type II $(Bi_2O_3)_{0.795}(Nb_2O_5)_{0.205}$. This material is available free of charge via the Internet at http://pubs.acs.org.

dx.doi.org/10.1021/ja3109328 | J. Am. Chem. Soc. 2013, 135, 6477–6484

AUTHOR INFORMATION

Corresponding Author

chris.ling@sydney.edu.au

Present Addresses

△The Bragg Institute, ANSTO, PMB 1, Menai 2234, Australia. ^School of Chemistry, University of New South Wales, Sydney 2052, Australia

Notes

The authors declare no competing financial interests.

ACKNOWLEDGMENTS

This work was supported by the Australian Research Council—Discovery Projects, the Australian Institute of Nuclear Science and Engineering Postgraduate Research Awards scheme, the Australian Synchrotron, and the FCT, Portugal. The authors thank Didier Richard of the ILL for reconstructing the neutron precession image shown in Figure 1, and Peter Turner of the University of Sydney for collecting X-ray diffraction data.

REFERENCES

(1) Jacobson, A. J. *Chem. Mater.* **2010**, *22*, 660.
(2) Orera, A.; Slater, P. R. *Chem. Mater.* **2010**, *22*, 675.
(3) Tarancon, A. *Energies* **2009**, *2*, 1130.
(4) Takahashi, T.; Iwahara, H. *Mater. Res. Bull.* **1978**, *13*, 1447.
(5) Harwig, H. A.; Gerards, A. G. *J. Solid State Chem.* **1978**, *26*, 265.
(6) Strickler, D. W.; Carlson, W. G. *J. Am. Ceram. Soc.* **1964**, *47*, 122.
(7) Kilner, J. A. *Chem. Lett.* **2008**, *37*, 1012.
(8) Drache, M.; Roussel, P.; Wignacourt, J. P. *Chem. Rev.* **2007**, *107*, 80.
(9) Lee, K. T.; Yoon, H. S.; Wachsman, E. D. *J. Mater. Res.* **2012**, *27*, 2063.
(10) Ling, C. D.; Withers, R. L.; Schmid, S.; Thompson, J. G. *J. Solid State Chem.* **1998**, *137*, 42.
(11) Sammes, N. M.; Tompsett, G. A.; Nafe, H.; Aldinger, F. *J. Eur. Ceram. Soc.* **1999**, *19*, 1801.
(12) Punn, R.; Feteira, A. M.; Sinclair, D. C.; Greaves, C. *J. Am. Chem. Soc.* **2006**, *128*, 15386.
(13) Kharton, V. V.; Naumovich, E. N.; Yaremchenko, A. A.; Marques, F. M. B. *J. Solid State Electrochem.* **2001**, *5*, 160.
(14) Takahashi, T.; Iwahara, H.; Esaka, T. *J. Electrochem. Soc.* **1977**, *124*, 1563.
(15) Tang, D.; Zhou, W. *J. Solid State Chem.* **1995**, *119*, 311.
(16) Withers, R. L.; Ling, C. D.; Schmid, S. *Z. Kristallogr.* **1999**, *214*, 296.
(17) Zhou, W.; Jefferson, D. A.; Thomas, J. M. *Proc. R. Soc. London, Ser. A* **1986**, *406*, 173.
(18) Struzik, M.; Malys, M.; Wrobel, W.; Abrahams, I.; Krok, F.; Dygas, J. R. *Solid State Ionics* **2011**, *202*, 22.
(19) Esmaeilzadeh, S.; Lundgren, S.; Halenius, U.; Grins, J. *J. Solid State Chem.* **2001**, *156*, 168.
(20) Valldor, M.; Esmaeilzadeh, S.; Pay-Gomez, C.; Grins, J. *J. Solid State Chem.* **2000**, *152*, 573.
(21) Yamamoto, A. *Acta Crystallogr., Sect. B: Struct. Sci.* **1982**, *38*, 1451.
(22) Bolotina, N. B. *Crystallogr. Rep.* **2006**, *51*, 968.
(23) van Smaalen, S.; Campbell, B. J.; Stokes, H. T. *Acta Crystallogr., Sect. A: Found. Crystallogr.* **2013**, *69*, 75.
(24) Battle, P. D.; Catlow, C. R. A.; Drennan, J.; Murray, A. D. *J. Phys. C: Solid State Phys.* **1983**, *16*, L561.
(25) Hull, S.; Norberg, S. T.; Tucker, M. G.; Eriksson, S. G.; Mohn, C. E.; Stolen, S. *Dalton Trans.* **2009**, 8737.
(26) Yashima, M.; Ishimura, D. *Chem. Phys. Lett.* **2003**, *378*, 395.
(27) Mohn, C. E.; Stolen, S.; Norberg, S. T.; Hull, S. *Phys. Rev. B* **2009**, *80*, 024205.
(28) Mohn, C. E.; Stolen, S.; Norberg, S. T.; Hull, S. *Phys. Rev. Lett.* **2009**, *102*, 155502.
(29) Miida, R.; Tanaka, M. *Jap. J. Appl. Phys., Part 1* **1990**, *29*, 1132.
(30) Joshi, A. V.; Kulkarni, S.; Nachlas, J.; Diamond, J.; Weber, N.; Virkar, A. V. *J. Mater. Sci.* **1990**, *25*, 1237.
(31) Meng, G. Y.; Chen, C. S.; Han, X.; Yang, P. H.; Peng, D. K. *Solid State Ionics* **1988**, *28*, 533.
(32) Yaremchenko, A. A.; Kharton, V. V.; Naumovich, E. N.; Vecher, A. A. *J. Solid State Electrochem.* **1998**, *2*, 146.
(33) Valant, M.; Suvorov, D. *J. Am. Ceram. Soc.* **2003**, *86*, 939.
(34) Osterloh, F. E. *Chem. Mater.* **2008**, *20*, 35.
(35) Zou, Z. G.; Ye, J. H.; Arakawa, H. *Chem. Mater.* **2001**, *13*, 1765.
(36) Pirnat, U.; Valant, M.; Jancar, B.; Suvorov, D. *Chem. Mater.* **2005**, *17*, 5155.
(37) Wang, X. P.; Corbel, G.; Kodjikian, S.; Fang, Q. F.; Lacorre, P. *J. Solid State Chem.* **2006**, *179*, 3338.
(38) Ling, C. D.; Johnson, M. *J. Solid State Chem.* **2004**, *177*, 1838.
(39) Roth, R. S.; Waring, J. L. *J. Res. Natl. Bur. Stand., Sect. A* **1962**, *66*, 451.
(40) Kharton, V. V.; Marques, F. M. B. *Solid State Ionics* **2001**, *140*, 381.
(41) Ravel, B.; Newville, M. *J. Synchrotron Radiat.* **2005**, *12*, 537.
(42) Petříček, V.; Dušek, M.; Palatinus, L. *Jana2006. The crystallographic computing system*; Institute of Physics: Praha, Czech Republic, 2006.
(43) Stokes, H. T.; Campbell, B. J.; van Smaalen, S. *Acta Crystallogr., Sect. A* **2011**, *67*, 45.
(44) Malys, M.; Holdynski, M.; Krok, F.; Wrobel, W.; Dygas, J. R.; Pirovano, C.; Vannier, R. N.; Capoen, E.; Abrahams, I. *J. Power Sources* **2009**, *194*, 16.
(45) Piilonen, P. C.; Farges, F.; Linnen, R. L.; Brown, G. E.; Pawlak, M.; Pratt, A. *Can. Mineral.* **2006**, *44*, 775.
(46) Ichikuni, N.; Iwasawa, Y. *J. Phys. Chem.* **1994**, *98*, 11576.
(47) Ling, C. D. *J. Solid State Chem.* **1999**, *148*, 380.
(48) Moreira, R. L.; Matinaga, F. M.; Pirnat, U.; Suvorov, D.; Dias, A. *J. Appl. Phys.* **2008**, *103*, 094108.
(49) Andersson, S.; Hyde, S. T.; Von Schnering, H. G. *Z. Kristallogr.* **1984**, *168*, 1.
(50) Von Schnering, H. G.; Nesper, R. *Z. Phys. B: Condens. Matter* **1991**, *83*, 407.
(51) van Smaalen, S. *Incommensurate Crystallography*; Oxford University Press: Oxford, UK, 2007.
(52) Brese, N. E.; O'Keeffe, M. *Acta Crystallogr., Sect. B* **1991**, *47*, 192.
(53) Ling, C. D. *Phys. B (Amsterdam, Neth.)* **2006**, *385*, 193.
(54) Ling, C. D.; Withers, R. L.; Thompson, J. G.; Schmid, S. *Acta Crystallogr., Sect. B* **1999**, *55*, 306.
(55) Buttrey, D. J.; Vogt, T.; Yap, G. P. A.; Rheingold, A. L. *Mater. Res. Bull.* **1997**, *32*, 947.
(56) Sharma, N.; Macquart, R. B.; Christensen, M.; Avdeev, M.; Chen, Y. S.; Ling, C. D. *J. Solid State Chem.* **2009**, *182*, 1312.